Precise Tailoring of Lithium-Ion Transport for Ultralong-Cycling Dendrite-Free All-Solid-State Lithium Metal Batteries

Weihan Li, James A. Quirk, Minsi Li, Wei Xia, Lucy M. Morgan, Wen Yin, Matthew Zheng, Leighanne C. Gallington, Yang Ren, Ning Zhu, Graham King, Renfei Feng, Ruying Li, James A. Dawson,* Tsun-Kong Sham,* and Xueliang Sun*

All-solid-state lithium metal batteries can address crucial challenges regarding insufficient battery cycling life and energy density. The demonstration of long-cycling dendrite-free all-solid-state lithium metal batteries requires precise tailoring of lithium-ion transport of solid-state electrolytes (SSEs). In this work, a proof of concept is reported for precise tailoring of lithium-ion transport of a halide SSE, Li_3InCl_6, including intragranular (within grains) but also intergranular (between grains) lithium-ion transport. Lithium-ion migration tailoring mechanism in crystals is developed by unexpected enhanced Li, In, and Cl vacancy populations and lower energy barrier for hopping. The lithium-ion transport tailoring mechanism between the grains is determined by the elimination of voids between grains and the formation of unexpected supersonic conducting grain boundaries, boosting the lithium dendrite suppression ability of SSE. Due to boosted lithium-ion conduction and dendrite-suppression ability, the all-solid-state lithium metal batteries coupled with Ni-rich $LiNi_{0.83}Co_{0.12}Mn_{0.05}O_2$ cathodes and lithium metal anodes demonstrate breakthroughs in electrochemical performance by achieving extremely long cycling life at a high current density of 0.5 C (2000 cycles, 93.7% capacity retention). This concept of precise tailoring of lithium-ion transport provides a cost, time, and energy efficient solution to conquer the remaining challenges in all-solid-state lithium-metal batteries for fast developing electric vehicle markets.

1. Introduction

All-solid-state lithium metal batteries provide a potential solution to overcoming the primary problems encountered in conventional lithium-ion batteries, which are prone to safety issues due to flammable liquid electrolytes, limited voltages, unstable cycling stability, and unsatisfactory energy density.[1] Additionally, the utilization of lithium metal anodes and high-capacity cathode materials in all-solid-state lithium metal batteries have promising capacity to deliver improved energy densities of >500 Wh kg^{-1}, thereby meeting key demands of electric vehicles for longer driving ranges.[2] It is therefore crucial to apply superionic conducting solid-state electrolytes (SSEs), tailor multiscale lithium-ion transport, and enhance suppression ability against lithium dendrite growth and penetration to enable the full potential of all-solid-state lithium metal batteries.

To obtain high ionic conductivity, intensive efforts are devoted to the innovation of compositions, crystal and local

W. Li, M. Li, M. Zheng, R. Li, X. Sun
Department of Mechanical and Materials Engineering
Western University
London, ON N6A 5B9, Canada
E-mail: xsun@eng.uwo.ca
W. Li, M. Li, T.-K. Sham
Department of Chemistry and Soochow-Western Centre for Synchrotron Radiation Research
Western University
London, ON N6A 5B7, Canada
E-mail: tsham@uwo.ca

J. A. Quirk, J. A. Dawson
Chemistry – School of Natural and Environmental Sciences
Newcastle University
Newcastle upon Tyne NE1 7RU, UK
E-mail: james.dawson@newcastle.ac.uk
L. M. Morgan
The Faraday Institution
Didcot OX11 0RA, UK
W. Xia, X. Sun
Eastern Institute for Advanced Study
Eastern Institute of Technology
Ningbo, Zhejiang 315201, China

structures, unraveling lithium-ion diffusion mechanisms, and the computational screening of new materials.[3–6] Lithium ions undergo multiscale transport, including the atomic scale (hopping between adjacent interstitial sites within grains) and micro and mesoscopic scales (transport through and between grains), as illustrated in **Figure 1A**.[4] Regarding the electrochemical performance of all-solid-state lithium-ion batteries, the lithium-ion transport manifesting at atomic, micro and mesoscopic scales is not only affected by the inherent crystal structures (i.e., grains) but also grain boundaries and voids.[7] In the case of the intragranular (within grains) lithium-ion transport, the lithium-ion conduction mainly depends on the concentration of mobile ions, hopping energy barrier (E_{Hop}), and hopping attempt frequency (v_{Hop}), which can be described by the Arrhenius relationship.[8] These factors relate to the crystal structures and local coordination environments, such as anionic frameworks, defects (e.g., vacancy-induced fast lithium-ion transport), and compositions.[9–11] For intergranular (between grains) lithium-ion transport, voids and grain boundaries are two main features that influence lithium-ion migration. Voids are ionic insulators and block lithium-ion transport. Similarly, grain boundaries are generally considered to increase the resistance of lithium-ion transport and the resistance depends on the SSE compositions.[7,12,13] The formation of superionic conducting grain boundaries can therefore further boost the ionic conductivity of SSEs. Additionally, voids and cracks between grains and poor ionically conducting grain boundaries are considered as the origins of serious lithium dendrite growth and penetration in SSEs which results in fast capacity fading and even internal short circuit and safety issues (see Figure 1B).[14–16] Therefore, it is crucial to screen and explore appropriate SSEs and to further precisely tailor multiscale (including intragranular and intergranular) lithium-ion conduction by eliminating voids and cracks and form superionic conducting grain boundaries between grains to enhance suppression ability against lithium dendrite growth and penetration via cost,

W. Yin
Institute of High Energy Physics
Chinese Academy of Sciences (CAS)
Beijing 100049, China

L. C. Gallington
X-Ray Science Division
Argonne National Laboratory
Argonne, IL 60439, USA

Y. Ren
Department of Physics
City University of Hong Kong
Kowloon, Hong Kong 999077, China

Y. Ren
Centre for Neutron Scattering
City University of Hong Kong
Kowloon, Hong Kong 999077, China

N. Zhu, G. King, R. Feng
Canadian Light Source
44 Innovation Boulevard
Saskatoon, Saskatchewan S7N 2V3, Canada

J. A. Dawson
Centre for Energy
Newcastle University
Newcastle upon Tyne NE1 7RU, UK

time, and energy efficient methods to make breakthroughs in electrochemical performance of all-solid-state lithium metal batteries.

In this work, we report a proof of concept for precise tailoring of multiscale lithium-ion transport in SSEs that demonstrates long-cycle-life dendrite-free all-solid-state lithium metal batteries. The enhanced multiscale lithium-ion transport can boost the ionic conductivity of Li_3InCl_6 at room temperature by around one order of magnitude from 6.95×10^{-4} to 4.4×10^{-3} S cm^{-1}. The underlying mechanism that boosts multiscale lithium-ion transport manifesting at the atomic, micro, and mesoscopic scales is unveiled by the studying crystal and local disorder structures within grains and voids and grain boundaries between grains. The enhancement in lithium-ion transport within grains can be attributed to the reduction in hopping energy, which arises from the evolution of the coordination environment. This unexpected evolution is associated with increased vacancy populations of lithium (Li), indium (In), and chloride (Cl) within the grains. To elucidate this mechanism, we employed a combination of synchrotron-based X-ray diffraction (SXRD) and time-of-flight (TOF) Neutron diffraction techniques, supplemented by large-scale molecular dynamics (MD) simulations, to refine both the crystal and local structures. The origin of the boosted lithium-ion conduction between grains is attributable to the formation of grain boundaries with unexpected high ionic conductivity and the elimination of voids, as observed by synchrotron-based X-ray computed tomography (XCT), and MD simulations. Additionally, the elimination of voids and the formation of superionic conducting grain boundaries between grains endow the SSEs with enhanced suppression ability against lithium dendrite growth and penetration (see Figure 1B). Owing to the boosted multiscale ionic conductivity and suppression ability against lithium dendrites, we demonstrate a long-cycle-life dendrite-free all-solid-state lithium metal battery design with Ni-rich $LiNi_{0.83}Co_{0.12}Mn_{0.05}O_2$ (NCM83) cathodes and lithium metal anodes, which present excellent electrochemical performance and an extremely long cycling life (capacity retention of 82.2% over 300 cycles for 0.1 C and 93.7% over 2000 cycles for 0.5 C).

2. Results and Discussion

2.1. Precise Tailoring of the Lithium-Ion Transport of Li_3InCl_6

The lithium-ion conductivity of Li_3InCl_6 at the SSE layer was precisely tailored using cold-pressing and hot-pressing methods. As shown in **Figure 2**; and Figure S1 (Supporting Information), the lithium-ion conductivity of cold-pressed and hot-pressed Li_3InCl_6 was evaluated using alternating current (AC) impedance. As shown in Figure S1A (Supporting Information), the room-temperature (i.e., 25 °C) ionic conductivity of the Li_3InCl_6 thin-layer film increased from 6.95×10^{-4} S cm^{-1} when pressed under 0.125 GPa to 1.1×10^{-3} S cm^{-1} with the pressure increased to 0.5 GPa. The room-temperature ionic conductivity remained at $\approx 1.1 \times 10^{-3}$ S cm^{-1} with the processing pressure was further increased from 0.5 to 0.75 GPa, meaning that the pressure of 0.5 GPa helped to realize the highest ionic conductivity during the cold-pressing process. With this optimized pressure of 0.5 GPa, the hot-pressing process was utilized to further improve
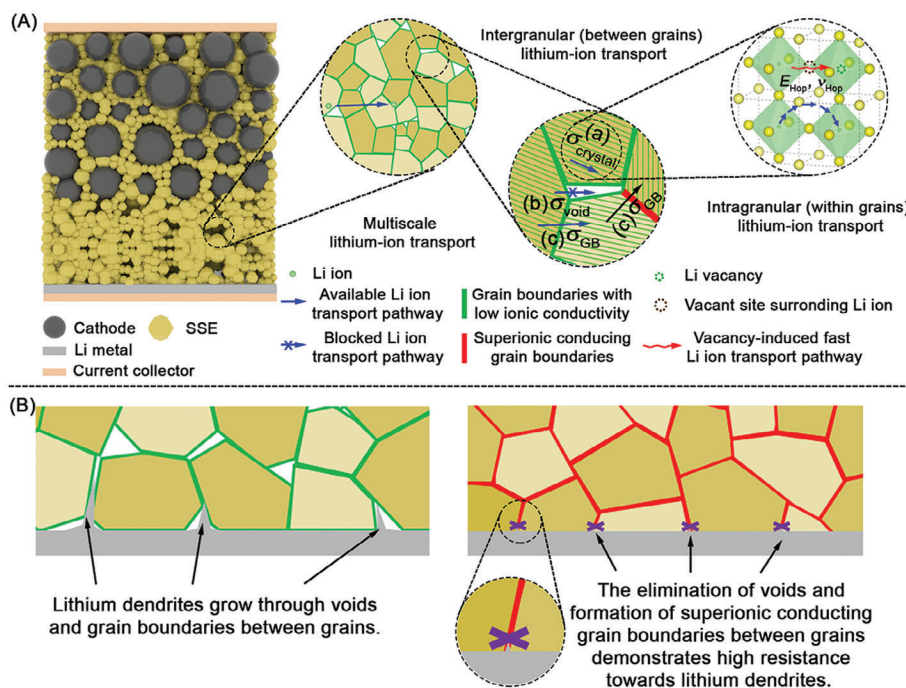
**ADVANCED
SCIENCE NEWS**

www.advancedsciencenews.com

**ADVANCED
MATERIALS**

www.advmat.de

Figure 1. Schematic illustration of A) multiscale lithium-ion transport in all-solid-state lithium metal batteries, including lithium-ion transport (a) within grains (crystal structures), (b) blocked by voids, and (c) through gain boundaries (two types: grain boundaries with low and high ionic conductivity) and B) lithium dendrite growth in solid-state electrolytes.

the room-temperature ionic conductivity, as shown in Figure S1B (Supporting Information). The room-temperature ionic conductivity increased from 1.1×10^{-3} S cm^{-1} for the cold-pressed film under 0.5 GPa to 1.68×10^{-3} S cm^{-1} after the hot-pressing process at 0.5 GPa and 100 °C. When the hot-pressing temperature was increased from 100 to 250 °C, the room-temperature ionic conductivity further increased to 4.4×10^{-3} S cm^{-1}, thereby outperforming most halide SSEs, including previously reported Li$_3$InCl$_6$ results.[17–19] After the hot-pressing temperature reached the range of 300−400 °C, the ionic conductivity of hot-pressed Li$_3$InCl$_6$ displayed a sudden drop to 10^{-7}−10^{-8} S cm^{-1}, suggesting the decomposition of Li$_3$InCl$_6$. The structural evolution and decomposition of Li$_3$InCl$_6$ during the hot-pressing process is discussed in detail later. The Arrhenius plots of cold- and hot-pressed Li$_3$InCl$_6$ are shown in Figure 2A. The activation energy was calculated based on the Arrhenius equation, as shown in Figure 2B; and Figure S1C,S1D (Supporting Information). According to the optimal pressing conditions, the activation energy is reduced from around 0.38 eV (cold-pressing process, 0.125 GPa) to 0.32 eV (hot-pressing process, 0.5 GPa-250 °C) with higher processing pressures and temperatures, suggesting that the hot-pressing process increase lithium-ion transport in Li$_3$InCl$_6$.

2.2. Intragranular Lithium-Ion Transport Tailoring Mechanism Within Grains at the Atomic Scale

The tailoring of lithium-ion transport mechanism at the atomic scale within grains is unraveled by the refinement of the crystal

and coordination structures of Li$_3$InCl$_6$ and through atomistic modeling.

Operando and ex situ SXRD were conducted to study the evolution of the crystal and local coordination structures of Li$_3$InCl$_6$, as shown in **Figures** 2C-F and 3A-D. The evolution of the XRD patterns of Li$_3$InCl$_6$ during the heating process from 25 to 400 °C without the pressing process was investigated in real time by operando SXRD, as shown in Figure 2C. At the beginning of the heating process, Li$_3$InCl$_6$ (i.e., heating-25 °C) presented a typical XRD pattern (ICSD No. 04-009-9027), as shown in Figure 2E. During the heating process, the XRD peaks belonging to Li$_3$InCl$_6$ gradually shifted toward a low 2θ angle without new peaks appeared, as shown in Figure 2C,E, suggesting that Li$_3$InCl$_6$ experienced a unit cell expansion during the heating process without self-decomposition and the formation of new phases. In the case of the following cooling process from 400 to 25 °C, the continuous shift of XRD peaks belonging to Li$_3$InCl$_6$ to a high 2θ angle was due to the shrinking of unit cells during the cooling process. After cooling down to 25 °C, Li$_3$InCl$_6$ (i.e., cooling-25 °C) showed no shift of XRD peaks compared to the pristine Li$_3$InCl$_6$ (i.e., heating-25 °C) but increase in the intensities of the XRD peaks, indicating the effect of annealing at 400 °C on the crystals. In the case of the hot-pressing process, the optimized pressing pressure and heating temperature induce similar annealing effect on Li$_3$InCl$_6$ with the increase of XRD peaks intensity as shown in Figure 2F. However, Li$_3$InCl$_6$ displayed decomposition to LiCl and InCl$_3$ with hot-pressing process up to 400 °C, according to the sudden drop in the room-temperature ionic conductivity when the temperature of hot-pressing process increases to higher than 300 °C, as shown in Figure S1B (Supporting Information). The difference between the operando SXRD result in
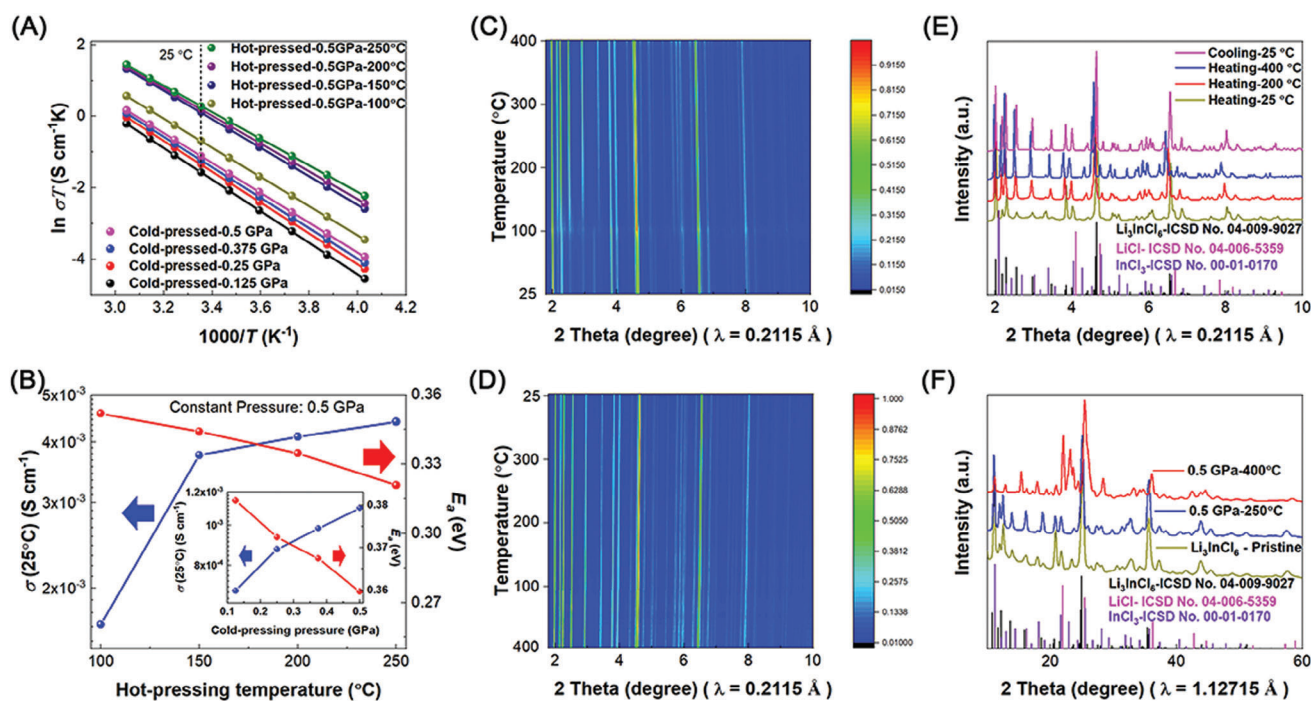
**ADVANCED
SCIENCE NEWS**

www.advancedsciencenews.com

**ADVANCED
MATERIALS**

www.advmat.de

Figure 2. A) Arrhenius plots of cold-pressed Li_3InCl_6 and hot-pressed Li_3InCl_6. B) Ionic conductivity at 25 °C (σ (25 °C)) and activation energy (E_a) of Li_3InCl_6 as a function of hot-pressing temperature with a constant pressure of 0.5 GPa and cold-pressing pressure (the insert figure). Operando SXRD of Li_3InCl_6 during C) heating process from 25 to 400 °C and D) following cooling process from 400 to 25 °C. E) SXRD patterns of during the heating and cooling process, heating-25, 300, and 400 °C, and cooling-25 °C. F) SXRD patterns of pristine Li_3InCl_6 and Li_3InCl_6 after the hot-processing processes, 0.5 GPa-250 °C, and 0.5 GPa-400 °C.

Figure 2E and ex situ SXRD results in Figure 2F is related to the different heating conditions. In the case of operando SXRD, Li_3InCl_6 was sealed in quartz tubes with ambient pressure, while Li_3InCl_6 was pressed in a die mold with metal pillars that then went through the hot-pressing process for ex situ SXRD testing. The decomposition of Li_3InCl_6 resulting from the hot-pressing process at high temperature might be due to the reaction between Li_3InCl_6 and the metal plungers.

To elucidate the mechanisms related to crystal and local coordination structural evolution enhancing lithium-ion transport at the atomic scale, Li_3InCl_6 was subjected to analysis using SXRD and TOF Neutron diffraction. Emphasis was placed on refining the crystal structures associated with Li, In, and Cl vacancies, as well as the cell parameters, utilizing the Rietveld method (see Figure 3A,B; and Figure S2, Supporting Information). Comprehensive structural data and details of the Rietveld refinement are presented in Tables S2–S5 (Supporting Information). As depicted in Figure 3C,D, the optimized hot-pressing process yielded increased Li and In vacancy concentrations in Li_3InCl_6-0.5 GPa-250 °C (28.6(2)% for Li vacancies and 45.6(5)% for In(1) 4 g sites) compared to the pristine Li_3InCl_6, which exhibited 38.0(2)% In and 24.1(6)% Li vacancy concentrations. Additionally, the hot-pressing process facilitated the creation of Cl vacancies, yielding concentrations of 8.6(4)% at Cl(1) 8j sites and 12.5(2)% at Cl(2) 4i sites. It should also be noted that the cell volume and interatomic distances within the crystal structure expanded as a result of the optimized hot-pressing process. The unit cell volume increased from 425.92(9) Å³ for pristine Li_3InCl_6, to 429.14(2) Å³ for the

Li_3InCl_6-0.5 GPa-250 °C as shown in Tables S2 and S4 (Supporting Information). Regarding the interatomic distances, the Cl-Cl and In-In interatomic distances increase to 3.9557 and 3.7761 Å after the optimized hot-pressing process, respectively compared to that of pristine Li_3InCl_6 (3.63 Å for Cl-Cl and 3.768 Å for In-In). The increase in Li, In, and Cl vacancy population and the enlargement of the cell volume and interatomic distances provide more space and reduce the energy barrier for lithium-ion diffusion at the atomic scale. The reduction in lithium-ion migration energy barrier also reduced the activation energy from 0.38 eV for the cold-pressed Li_3InCl_6 under 0.125 GPa to 0.32 eV for the hot-pressed Li_3InCl_6 under 0.5 Gpa-250 °C and significantly boosted the room-temperature ionic conductivity from 6.95×10^{-4} to 4.4×10^{-3} S cm^{-1}.

Atomistic modeling was used to verify our experimental findings and further explore the role that crystal and local coordination structures have on lithium-ion transport in Li_3InCl_6. We calculated the lithium-ion conductivities (see Figure 3E) of bulk (single-crystal) Li_3InCl_6 systems with the compositions of the cold- and hot-pressed samples ($Li_{4.556(4)}In_{2.481(3)}Cl_{12}$ and $Li_{4.313(1)}In_{2.176(2)}Cl_{10.809(5)}$, respectively) using MD, as described in the Computational methods section (see the Supporting Information). From Figure 3E, we see that a higher lithium-ion conductivity (6.37×10^{-4} S cm^{-1} at 300 K) and reduced activation energy (0.30 eV) is achievable by hot-pressing compared to cold-pressing (3.09×10^{-4} S cm^{-1} and 0.33 eV, respectively), in excellent agreement with our experimental results and previous ab initio MD simulations.[20] These findings show that an increase in
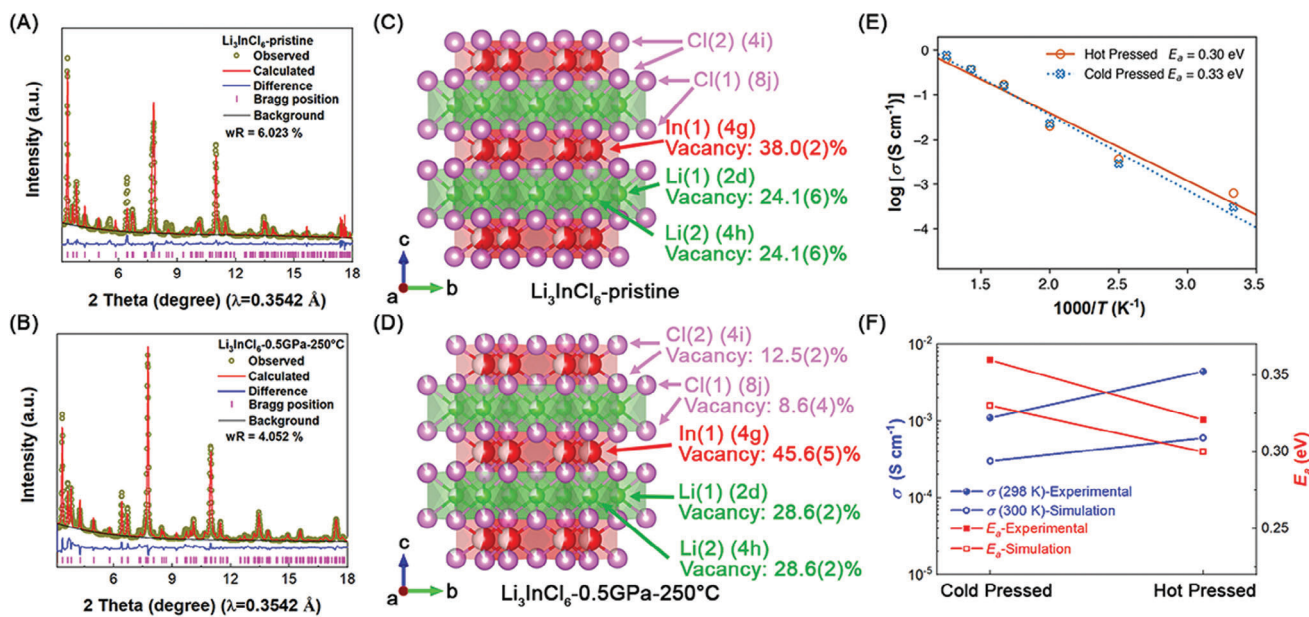
**ADVANCED
SCIENCE NEWS**

www.advancedsciencenews.com

**ADVANCED
MATERIALS**

www.advmat.de

Figure 3. Synchrotron-based X-ray diffraction pattern and corresponding Rietveld refinement of A) pristine Li_3InCl_6 and B) Li_3InCl_6-0.5GPa-250 °C. Refined crystal structures of C) pristine Li_3InCl_6 and D) Li_3InCl_6-0.5GPa-250 °C. E) Calculated lithium-ion conductivities for hot- and cold-pressed Li_3InCl_6 F) Comparison of ionic conductivities (σ) and activation energy (E_a) for hot- and cold-pressed Li_3InCl_6 from simulations and experimental measurements.

the In vacancy concentration (as found for the hot-pressed sample) is beneficial for lithium-ion transport. In accordance with our experimental setup, we also investigated the effect of using a pressure of 0.5 GPa in the MD simulations on the lithium-ion transport. However, this relatively small change in pressure to 0.5 GPa had a negligible effect on the lithium-ion conductivity in the simulations.

2.3. Intergranular Lithium-Ion Transport Tailoring Mechanism Between Grains at the Micro and Mesoscopic Scales

The tailoring of lithium-ion transport mechanism at the micro and mesoscopic scales between grains are presented by visualizing interior features within Li_3InCl_6 and simulations of lithium-ion conduction.

Generally, voids are formed between grains and result in lower densities compared to perfect single crystals, suggesting that relative density is the key feature to represent void population within pressed Li_3InCl_6. The relative densities of cold-pressed and hot-pressed Li_3InCl_6 were calculated as shown in **Figure 4A**. Under the cold-pressing process, the relative density of Li_3InCl_6 increased from 59.16% with a low pressure of 0.125 GPa to 80.29% with a high pressure of 0.5 GPa and then remained at 80.3% with further higher pressures up to 0.75 GPa. The hot-pressing process helped to further increase the relative density Li_3InCl_6 thin-layer films up to 93.67% with the optimized pressure and temperature (0.5 GPa-250 °C). By comparing Figures S1A,B and S4A (Supporting Information), the evolution of room-temperature ionic conductivity under the cold- and hot-pressing processes is consistent with that of relative density. Furthermore, as shown in Figure 4B, the higher relative density induced higher

room-temperature ionic conductivity and lower activation energy. The morphology of cold- and hot-pressed Li3InCl6 was detected by scanning electron microscopy (SEM) (see Figure 4C,F) and synchrotron-based XCT (see Figure 4D,E,G,H). The cold-pressed Li_3InCl_6 under 0.5 GPa shows numerous cracks and voids, which block lithium-ion transport between grains (see Figure 1) and thus restricts high ionic conductivity. In contrast, the hot-pressing process with the same pressing pressure and heating process under 250 °C eliminates the voids between grains and hot-pressed Li_3InCl_6 displays tight connection between grains, which helps lithium ion to transport smoothly and rapidly between grains and thus trigger high room-temperature ionic conductivity. Comparing the evolution of relationship between relative density and room-temperature ionic conductivity or activation energy under the cold- and hot-pressing processes, there is an abrupt change when the relative density increases from 80.29% with the cold-pressing process of 0.5 GPa to 93.67% with the hot-pressing process of 0.5 GPa-250 °C. This suggests that the hot-pressing process not only promotes lithium-ion transport at the atomic scale within grains owing to the increased In vacancy population, but also eliminates the resistance resulting from voids and finally boosts multiscale lithium-ion transport in Li_3InCl_6.

Given that our experimental analysis revealed that hot-pressed Li_3InCl_6 samples with high densities exhibited the highest lithium-ion conductivity, it is important to understand the role of grain boundaries in influencing lithium-ion transport in Li_3InCl_6. While it is well known that grain boundaries in oxide SSEs are usually highly resistive,[7,16] the nature of grain boundary resistance in halide SSEs is less well understood. The calculated lithium-ion conductivities for three representative Li_3InCl_6 grain boundaries (displayed in **Figure 5A**) are presented

**ADVANCED
SCIENCE NEWS**

www.advancedsciencenews.com
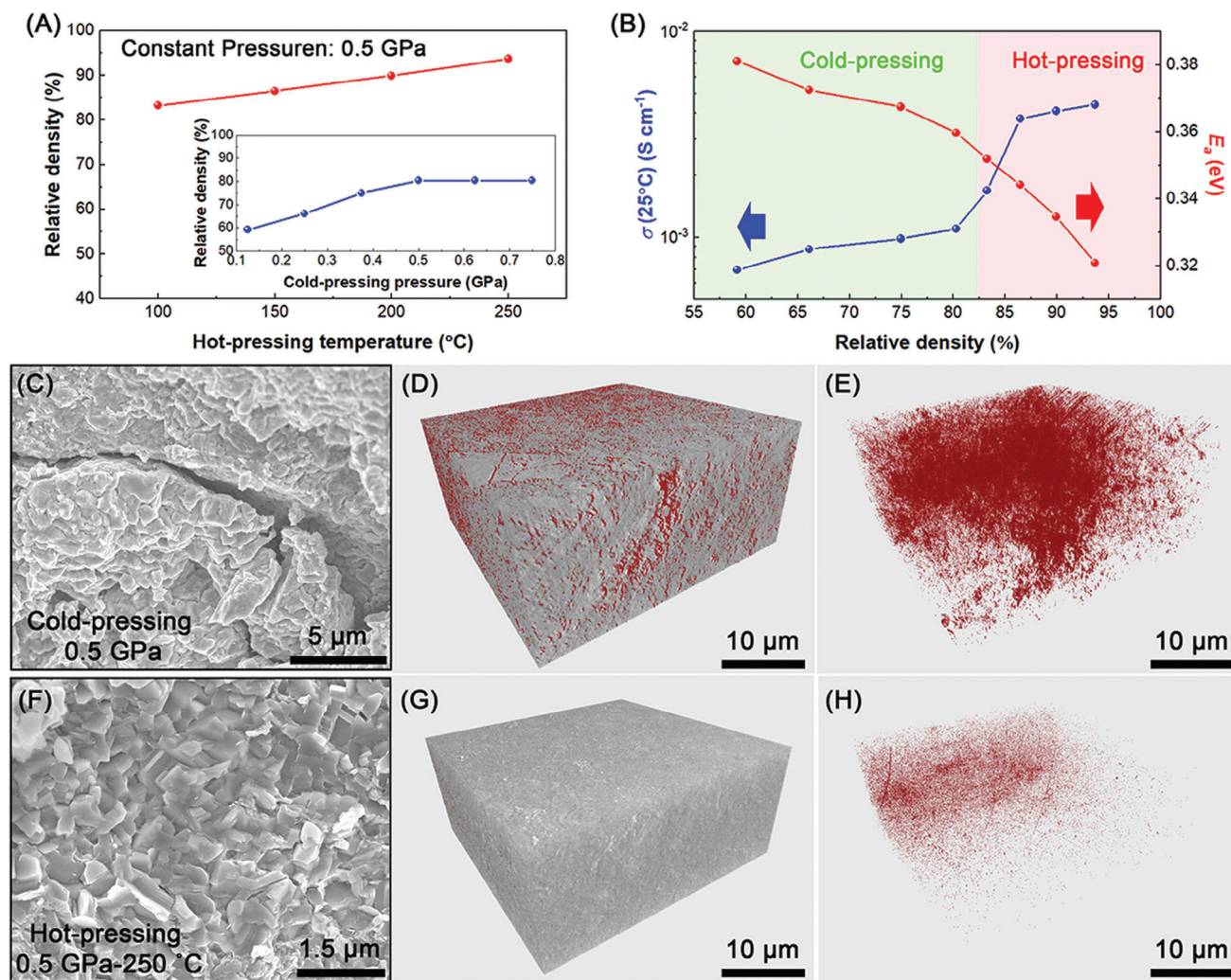
**ADVANCED
MATERIALS**

www.advmat.de

Figure 4. A) Relative densities of hot-pressed Li_3InCl_6 as a function of hot-pressing temperature with a constant pressure of 0.5 GPa with the insert shows the relationship between relative densities and cold-pressing pressure. B) Ionic conductivity at 25 °C (σ (25 °C)) and activation energy (E_a) of Li_3InCl_6 as a function of relative density. SEM images of Li_3InCl_6 under C) cold-pressing process of 0.5 GPa and (F) hot-pressing process of 0.5 GPa-250 °C. The 3D volume rendered images from the synchrotron-based X-ray computed tomography (XCT) of Li_3InCl_6 under D,E) cold-pressing process of 0.5 GPa and G,H) hot-pressing process of 0.5 GPa-250 °C. In the images, gray represents Li_3InCl_6 and red represents the cracks and voids. D,G) presents the virtual images of Li_3InCl_6 and cracks and voids together, while E,H) present voids.

in Figure 5B. The Li-ion conductivities of ≈1–3 × 10^{-4} S cm^{-1} at 300 K for the three grain boundaries are very similar to the value of 3.09 × 10^{-4} S cm^{-1} obtained for the cold-pressed sample, indicating that the presence of grain boundaries in this halide material does not significantly hinder its Li-ion transport. This is further supported by the marginal increase in activation energy (0.01–0.04 eV) for the grain boundaries compared to the cold- and hot-pressed samples. These findings are in accordance with our previous density functional theory simulations of the $\sum3\{112\}$ and $\sum5\{310\}$ Li_3InCl_6 grain boundaries, where it was revealed that these grain boundaries have only a minor influence on the electrostatic environment and correlated transport of Li ions in this material.[20]

Our experiments have revealed a clear relationship between Li-ion conductivity and relative density in Li_3InCl_6. To further verify and understand this relationship, we developed several large-scale Li_3InCl_6 models for MD simulations with relative atomic densities of 90%, 78%, and 66%, respectively, in agreement with our experimental cold- and hot-pressed samples. Examples of these models are presented in Figure 5C, where the level of voids is illustrated by the missing $LiCl_6$ and $InCl_6$ octahedra. The calculated Li-ion conductivities of these models are displayed as a function of relative density/void concentration, as given in Figure 5D. Several points emerge from these results. First, we observe a clear trend of increasing room-temperature Li-ion conductivity with increasing density, i.e., from ≈8 × 10^{-5} to ≈2 × 10^{-4} S cm^{-1} for an increase in density from 66% to 90%, respectively, which strongly agrees with the experimental findings. Second, there is an opposing trend regarding the activation energy for lithium-ion conductivity with density, i.e., a decrease from 0.41 to 0.35 eV is found for an increase in density from 66% to 90%, respectively. This again agrees with our experimental results, where a similar
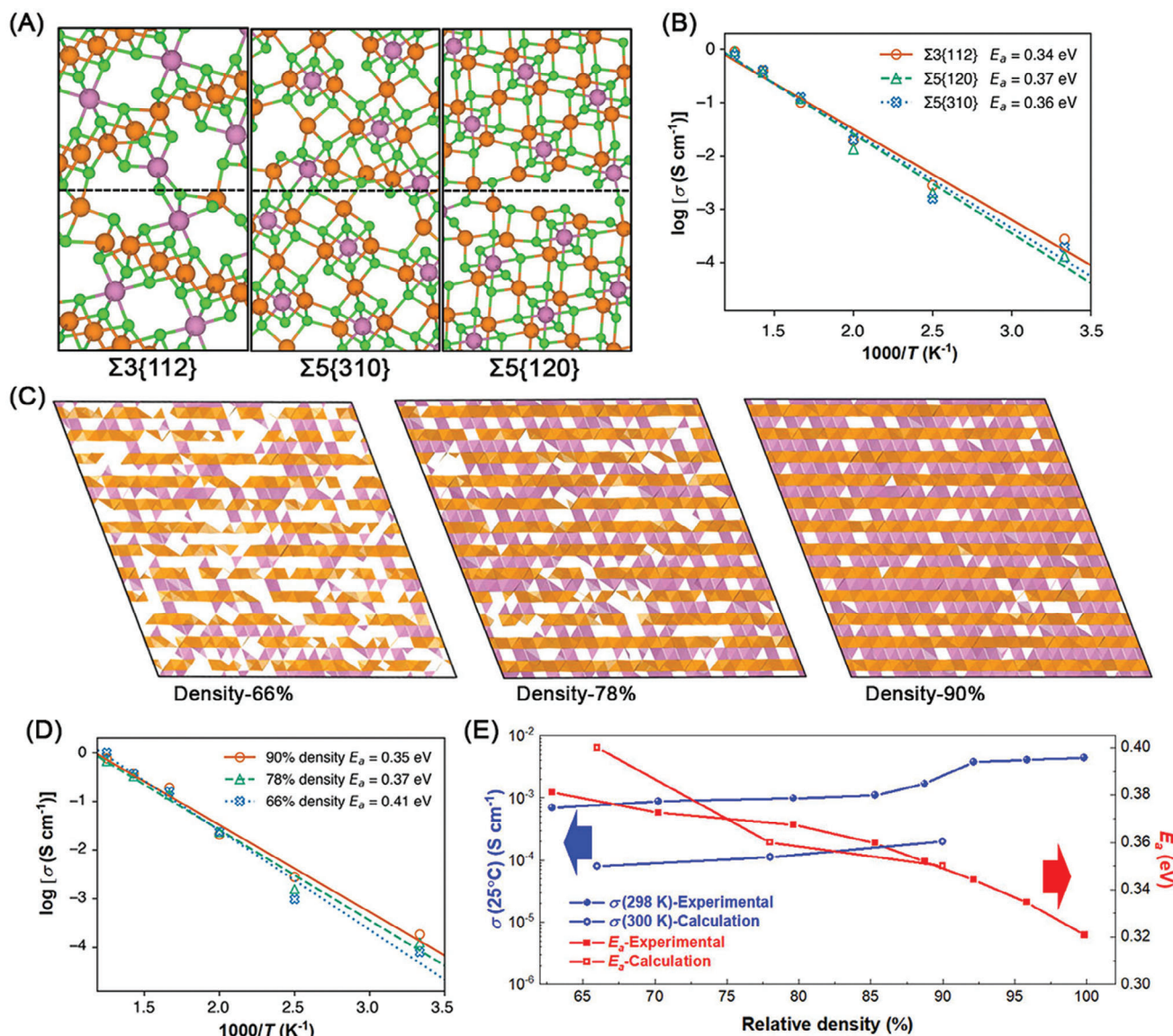
**ADVANCED
SCIENCE NEWS**

www.advancedsciencenews.com

**ADVANCED
MATERIALS**

www.advmat.de

Figure 5. A) Li_3InCl_6 grain boundary models. Lithium, indium, and chlorine are given in orange, purple, and green, respectively. Dashed lines indicate the grain boundaries. Calculated lithium-ion conductivities for B) Li_3InCl_6 grain boundaries and D) Li_3InCl_6 as a function of density. The corresponding activation energies, E_a, for each system are also shown. C) Li_3InCl_6 models with reduced atomic density (90%, 78%, and 66%, left to right). $LiCl_6$ and $InCl_6$ octahedra are given in orange and purple, respectively. E) Comparison of ionic conductivities (σ) and activation energy (E_a) for Li_3InCl_6 as a function of density from simulations and the experimental measurements.

decrease from 0.34 to 0.32 eV was determined. Third, these results suggest that the relative density induced by cracks and voids has a more significant effect on Li-ion transport in Li_3InCl_6 than the grain boundaries and illustrate the importance of maximizing the density and contact between grains for enhanced Li-ion conductivity in Li_3InCl_6 and potentially other halide SSEs.

2.4. Long-Cycle-Life All-Solid-State Lithium Metal Batteries

Due to the enhanced lithium-ion conduction, eradication of voids, and the establishment of superionic conducting grain boundaries, hot-pressed Li_3InCl_6 led to reduced battery

impedance and elevated electrochemical performance at high current densities, as illustrated in **Figure 6**. In Figures S3 and S4 (Supporting Information), it is evident that Li_3InCl_6 exhibits incompatibility with lithium metal, attributable to the emergence of mixed ionic and electronic interphases (such as In or Li-In alloy, and LiCl) at the Li_3InCl_6 and lithium metal interface. To mitigate this incompatibility, the sulfide-based SSE, Li_6PS_5Cl, was introduced as an interface for the lithium metal anode. As depicted in Figure S5 (Supporting Information), Li_6PS_5Cl demonstrates favorable compatibility with lithium metal, resulting from the formation of stable solid-electrolyte interphases, including Li-P alloy, Li_2S, and LiCl. Subsequently, we constructed all-solid-state lithium metal batteries using Li_3InCl_6-Li_6PS_5Cl (LIC-LPSCl) as
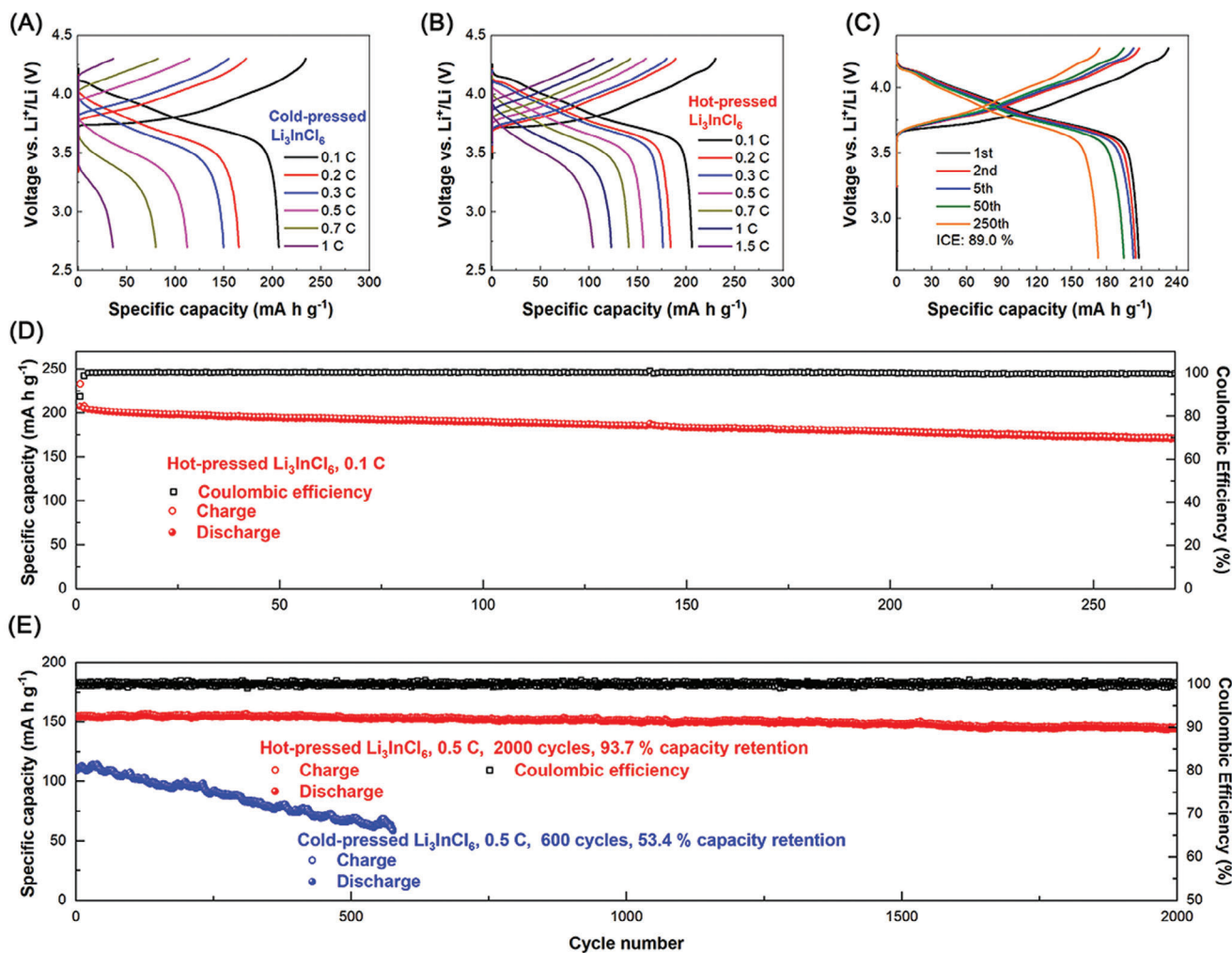
Figure 6. Long-term electrochemical performance of the NCM83-LIC-LPSCl-Li all-solid-state lithium metal batteries at 25 °C with an operating voltage window between 4.3 and 2.7 V. Charge/discharge curves at incremental cycling rates up to 1.5 C with A) cold-pressed Li_3InCl_6 and B) hot-pressed Li_3InCl_6 and C) 0.1 C with hot-pressed Li_3InCl_6. Charge–discharge capacity and the Coulombic efficiency as a function of cycle number for all-solid-state lithium metal batteries cycled at D) 0.1 C with hot-pressed Li_3InCl_6 and E) 0.5 C with comparison between hot-pressed Li_3InCl_6 and cold-pressed Li_3InCl_6.

the SSE, Ni-rich $LiNi_{0.83}Co_{0.11}Mn_{0.06}O_2$ (NCM83) as the cathode, and lithium metal as the anode, resulting in the NCM83-LIC-LPSCl-Li configuration. All-solid-state lithium metal batteries with cold-pressed Li_3InCl_6 displayed lower capacities at high current densities ($\approx$112 mAh g^{-1} at 0.5 C and only $\approx$35 mAh g^{-1} at 1.0 C, see Figure 6A). The unsatisfactory electrochemical performance is due to large overpotential at high current densities resulted from the lower ionic conductivity of cold-pressed Li_3InCl_6 and limited capability to prevent lithium dendrite growth and penetration due to high void and crack population in this SSE layer. In contrast, the all-solid-state batteries utilizing hot-pressed Li_3InCl_6 maintained high capacities at high current densities up to 1.5 C ($\approx$156 mAh g^{-1} at 0.5 C, $\approx$123 mAh g^{-1} at 1.0 C, and $\approx$104 mAh g^{-1} at 1.5 C, see Figure 6B). The mechanism for innovative electrochemical performance is owed to two factors. First, the boosted lithium-ion transport in hot-pressed Li_3InCl_6 within grains and between grains induced low battery device impedance and low charge/discharge overpotential at high current densities. Second, the elimination of voids and cracks in hot-pressed

Li_3InCl_6 SSE layer is the origin of high suppression ability to lithium dendrite growth and penetration in SSE layers. All-solid-state lithium metal symmetric cells using hot-pressed Li_3InCl_6 demonstrated higher suppression ability against lithium metal dendrites with much higher critical current densities and capacities of 4 mA cm^{-2} and 4 mAh cm^{-2} than that with single Li_6PS_5Cl (0.6 mA cm^{-2} and 0.6 mAh cm^{-2}), and cold-pressed Li_3InCl_6 (1.2 mA cm^{-2} and 1.2 mAh cm^{-2}) as shown in Figures S6 and S7 (Supporting Information). Additionally, all-solid-state lithium metal symmetric cells using hot-pressed Li_3InCl_6 also presented long cycling stability at 2 mA cm^{-2} and 2 mAh cm^{-2} for 3000 h (see Figure S7, Supporting Information). In solid-state batteries employing hot-pressed Li_3InCl_6, prolonged cycling lifetimes were observed at 0.1 C (270 cycles with 82.2% capacity retention) and 0.5 C (2000 cycles with 93.7% capacity retention). Figure 6C,D illustrates the voltage profile and cycling performance of the solid-state battery when cycled at 0.1 C within a voltage window of $\approx$2.7–4.3 V versus Li$^+$/Li. During the inaugural cycle, a notable reversible capacity of $\approx$207 mAh g^{-1} was

**ADVANCED
SCIENCE NEWS**

www.advancedsciencenews.com

**ADVANCED
MATERIALS**

www.advmat.de

achieved, complemented by a commendable initial Coulombic efficiency of 89.0%. The Coulombic efficiency ascended to nearly 100% subsequent to the first cycle, with the battery maintaining a robust capacity retention of 82.2% after 270 cycles. Cycling at 0.5 C, the all-solid-state batteries delivered a long cycling life with low capacity decay (see Figure 6E) with high capacity retention of 93.7% and reversible capacity of ≈149.2 mAh g^{-1} over 2000 cycles. The stable electrochemical performance of all-solid-state lithium metal batteries with hot-pressed Li_3InCl_6 indicates that boosted multiscale lithium-ion migration and low void and crack population in SSE layers help to achieve long cycling life.

3. Conclusion

In summary, we have demonstrated a concept that precise tailoring of lithium-ion transport in Li_3InCl_6 SSE enables long-cycle-life dendrite-free all-solid-state lithium metal batteries. The room-temperature lithium-ion conductivity increased by around one order of magnitude from 6.95×10^{-4} to 4.4×10^{-3} S cm^{-1}. The lithium-ion transport tailoring mechanism at atomic, micro, and mesoscopic scales can be attributed as follows. The enhanced intragranular lithium-ion conduction mechanism arises from a reduced lithium-ion hopping barrier energy, attributed to an unanticipated increase in the vacancy populations of Li, In, and Cl. This understanding was elucidated through refinement of both the crystal and local structures using SXRD, TOF-Neutron diffraction, and MD simulations. The origin of boosted intergranular Li-ion conduction mechanism is due to elimination of ionic-insulating voids and unexpected superionic conducting grain boundaries forming between grains, which was unraveled by XCT, and MD simulations. Owing to the boosted ionic conductivity, the elimination of voids, forming superionic conducting grain boundaries between grains and boosted lithium-dendrite suppression ability, we demonstrated a long-cycle-life all-solid-state lithium metal battery design with Ni-rich $LiNi_{0.83}Co_{0.12}Mn_{0.05}O_2$ cathodes and lithium metal anodes, which present excellent electrochemical performance and extremely long cycling life (capacity retention: 82.2% over 300 cycles for 0.1 C and 93.7% over 2000 cycles for 0.5 C). These findings make this work a crucial breakthrough in all-solid-state lithium metal batteries for the future development of electric vehicles.

Supporting Information

Supporting Information is available from the Wiley Online Library or from the author.

Conflict of Interest

All authors declare no conflicts of interest.

Author Contributions

W.L., J.A.Q, and M.L. contributed equally to this work. W.L. and X.S. conceived the idea. T.K.S. and X.S. supervised this work. W.L. and M.L. synthesized all the materials, performed, and analyzed electrochemical characterization. R.L. helped with the scanning electron microscopy. W.L. appreciates the funding support form Mitacs Accelerate Fellowships. W.L., M.L., M.Z., and N.Z. performed and analyzed synchrotron-based X-ray computed tomography. W.L., L.C.G., Y.R., G.K., and R.F. performed and analyzed synchrotron-based X-ray diffraction. W.X., W.Y., and W.L. performed and analyzed the Time-of-flight Neutron diffraction data. J.A.Q. and J.A.D. performed simulations and modeling. W.L., J.A.Q., and M.L. drafted the manuscript. All the authors discussed the results and commented on the manuscript preparation.

Data Availability Statement

The data that support the findings of this study are available from the corresponding author upon reasonable request.

[1] P. Albertus, V. Anandan, C. Ban, N. Balsara, I. Belharouak, J. Buettner-Garrett, Z. Chen, C. Daniel, M. Doeff, N. J. Dudney, B. Dunn, S. J. Harris, S. Herle, E. Herbert, S. Kalnaus, J. A. Libera, D. Lu, S. Martin, B. D. McCloskey, M. T. McDowell, Y. S. Meng, J. Nanda, J. Sakamoto, E. C. Self, S. Tepavcevic, E. Wachsman, C. Wang, A. S. Westover, J. Xiao, T. Yersak, *ACS Energy Lett.* **2021**, *6*, 1399.

[2] J. Liu, Z. Bao, Y. Cui, E. J. Dufek, J. B. Goodenough, P. Khalifah, Q. Li, B. Y. Liaw, P. Liu, A. Manthiram, Y. S. Meng, V. R. Subramanian, M. F. Toney, V. V. Viswanathan, M. S. Whittingham, J. Xiao, W. Xu, J. Yang, X.-Q. Yang, J.-G. Zhang, *Nat. Energy* **2019**, *4*, 180.

[3] Q. Zhao, S. Stalin, C.-Z. Zhao, L. A. Archer, *Nat. Rev. Mater.* **2020**, *5*, 229.

[4] T. Famprikis, P. Canepa, J. A. Dawson, M. S. Islam, C. Masquelier, *Nat. Mater.* **2019**, *18*, 1278.

[5] L. Kahle, A. Marcolongo, N. Marzari, *Energy Environ. Sci.* **2020**, *13*, 928.

[6] X. He, Y. Zhu, Y. Mo, *Nat. Commun.* **2017**, *8*, 15893.

[7] J. A. Dawson, P. Canepa, T. Famprikis, C. Masquelier, M. S. Islam, *J. Am. Chem. Soc.* **2018**, *140*, 362.

[8] J. C. Bachman, S. Muy, A. Grimaud, H.-H. Chang, N. Pour, S. F. Lux, O. Paschos, F. Maglia, S. Lupart, P. Lamp, L. Giordano, Y. Shao-Horn, *Chem. Rev.* **2016**, *116*, 140.

[9] Y. Wang, W. D. Richards, S. P. Ong, L. J. Miara, J. C. Kim, Y. Mo, G. Ceder, *Nat. Mater.* **2015**, *14*, 1026.

[10] X. He, Y. Zhu, Y. Mo, *Nat. Commun.* **2017**, *8*, 15893.

[11] K. Jun, Y. Sun, Y. Xiao, Y. Zeng, R. Kim, H. Kim, L. J. Miara, D. Im, Y. Wang, G. Ceder, *Nat. Mater.* **2022**, *21*, 924.

[12] J. A. Dawson, P. Canepa, M. J. Clarke, T. Famprikis, D. Ghosh, M. S. Islam, *Chem. Mater.* **2019**, *31*, 5296.

[13] K. Nakano, N. Tanibata, H. Takeda, R. Kobayashi, M. Nakayama, N. Watanabe, *J. Phys. Chem. C* **2021**, *125*, 23604.

[14] Z. Ning, D. S. Jolly, G. Li, R. De Meyere, S. D. Pu, Y. Chen, J. Kasemchainan, J. Ihli, C. Gong, B. Liu, D. L. R. Melvin, A. Bonnin, O. Magdysyuk, P. Adamson, G. O. Hartley, C. W. Monroe, T. J. Marrow, P. G. Bruce, *Nat. Mater.* **2021**, *20*, 1121.

[15] F. Han, A. S. Westover, J. Yue, X. Fan, F. Wang, M. Chi, D. N. Leonard, N. J. Dudney, H. Wang, C. Wang, *Nat. Energy* **2019**, *4*, 187.

[16] C. Ma, K. Chen, C. Liang, C. Nan, R. Ishikawa, K. More, M. Chi, *Energy Environ. Sci.* **2014**, *7*, 1638.

[17] X. Li, J. Liang, J. Luo, M. N. Banis, C. Wang, W. Li, S. Deng, C. Yu, F. Zhao, Y. Hu, T.-K. Sham, L. Zhang, S. Zhao, S. Lu, H. Huang, R. Li, K. R. Adair, X. Sun, *Energy Environ. Sci.* **2019**, *12*, 2665.

[18] X. Li, J. Liang, N. Chen, J. Luo, K. R. Adair, C. Wang, M. N. Banis, T.-K. Sham, L. Zhang, S. Zhao, S. Lu, H. Huang, R. Li, X. Sun, *Angew. Chem.* **2019**, *131*, 16579.

[19] T. Asano, A. Sakai, S. Ouchi, M. Sakaida, A. Miyazaki, S. Hasegawa, *Adv. Mater.* **2018**, *30*, 1803075.

[20] J. A. Quirk, J. A. Dawson, *Adv. Energy Mater.* **2023**, *13*, 2301114 .